A-site Mn^{2+} tuned magnetism and electrical transport properties in the transition-metal-only perovskite oxide $MnCu_3Mn_4O_{12}$

Jia Guo,[1,2] Suyun Wang,[3,4] Wenmin Li,[1] Dabiao Lu,[1,2] Xubin Ye,[1,2] Zhehong Liu,[1] Shijun Qin,[1,2] Xiao Wang,[5] Zhiwei Hu,[5] Hong-Ji Lin,[6] Chien-Te Chen,[6] Jianguo Wan,[4] Qinfang Zhang,[3,*] and Youwen Long[1,2,7,†]

[1] *Beijing National Laboratory for Condensed Matter Physics, Institute of Physics, Chinese Academy of Sciences, Beijing 100190, China*
[2] *School of Physical Sciences, University of Chinese Academy of Sciences, Beijing 100049, China*
[3] *School of Materials Science, Yancheng Institute of Technology, Yancheng 224051, China*
[4] *School of Physical Science, Nanjing University, Nanjing 210008, China*
[5] *Max Planck Institute for Chemical Physics of Solids, Dresden 01187, Germany*
[6] *National Synchrotron Radiation Research Center, Hsinchu 30076, Taiwan*
[7] *Songshan Lake Materials Laboratory, Dongguan, Guangdong 523808, China*

(Received 8 December 2021; accepted 28 January 2022; published 10 February 2022)

An $AA'_3B_4O_{12}$-type transition-metal-only quadruple perovskite oxide $MnCu_3Mn_4O_{12}$ was prepared by high-pressure and high-temperature methods. The compound has a cubic Im-3 symmetry with charge distribution of $Mn^{2+}Cu^{2+}_3Mn^{4+}_4O_{12}$. A long-range ferrimagnetic phase transition caused by $Cu^{2+}(\uparrow)Mn^{4+}(\downarrow)$ spin interaction is found to occur at a Curie temperature $T_C \approx 365$ K . Different from the isostructural compound $CaCu_3Mn_4O_{12}$, the susceptibility of $MnCu_3Mn_4O_{12}$ experiences a second anomaly ~200 K due to the effects of A-site Mn^{2+} spin ordering. Moreover, the A-site Mn^{2+} spins also considerably decrease the magnitude of resistivity. Theoretical calculations reveal that the A-site Mn $3d$ orbitals locate near the Fermi level and hybridize with the Cu $3d$ and O $2p$ orbitals, playing a crucial role on the magnetic and electrical transport properties of $MnCu_3Mn_4O_{12}$. In this paper, we provide an interesting example using A-site magnetic ions to significantly tune the physical properties in $AA'_3B_4O_{12}$-type quadruple perovskite oxides.

DOI: 10.1103/PhysRevB.105.054409

I. INTRODUCTION

A-site-ordered quadruple perovskite oxides with the chemical formula $AA'_3B_4O_{12}$ have been attracting remarkable interest due to fascinating structural and physical properties, such as intermetallic charge transfer [1–4], charge disproportionation [5–7], giant dielectric constant [8], magnetoelectric multiferroicity [9,10], negative thermal expansion [1,4], and highly efficient catalysis [11–13]. In this ordered structure, three quarters of the A site is usually filled with a transition metal (TM) ion A' with strong Jahn-Teller effect like Cu^{2+} or Mn^{3+}. Owing to the smaller A'-site ionic size, the BO_6 octahedra must heavily tilt to stabilize the perovskite structure [14]. A typical B-O-B bond angle is about 140 ° in $AA'_3B_4O_{12}$ perovskites. Since these compounds contain TM ions at both A' and B sites, there exist A'-A' and A'-B interactions in addition to the conventional B-B interactions as seen in simple ABO_3 perovskites, giving rise to striking magnetic and electrical behaviors. For example, the A'-A' spin interactions in $CaCu_3Ge_4/Sn_4O_{12}$ lead to rare ferromagnetic (FM) ordering of Cu^{2+} ions [15]. The A'-B interactions in $LaCu_3Fe_4O_{12}$ cause intermetallic charge transfer with sharp structural, magnetic, and electrical variations [1]. In $CaCu_3Mn_4O_{12}$ (CCMO), the A'-B interactions result in a long-range ferrimagnetic (FiM) ordering at $T_C \approx 355$ K. Moreover, a large room-temperature (RT) low-field magnetoresistance (MR) response without double exchange is found to occur due to the Cu(↑)Mn(↓) FiM coupling [16]. Chemical substitutions either at A/A' or B sites in $AA'_3B_4O_{12}$ perovskites can effectively modify the structural, magnetic, and transport properties. Specifically, A-site substitutions of rare earth for Ca^{2+} in $RCu_3Mn_4O_{12}$ (R = rare earth) can enhance the T_C as well as induce the MR response at low magnetic fields [17]. The divalent A-site cation for $ACu_3Mn_4O_{12}$ has been explored only in CCMO and $CdCu_3Mn_4O_{12}$ [18]. Different from the semiconducting conductivity of CCMO, metallic behavior is observed in $CdCu_3Mn_4O_{12}$ due to the increment of density of states (DOS) near the Fermi level.

Recently, it was revealed that not only the A' and B sites but also the A site can accommodate TM ions in A-site-ordered quadruple perovskite oxides, resulting in the formation of TM-only perovskites. Moreover, the A-site TM ions can also take part in the magnetism and electrical transport. To date, only a few TM-only quadruple perovskite oxides such as $Mn/CuCu_3V_4O_{12}$ and $MnMn_3Mn_4O_{12}$ (i.e., the ζ-Mn_2O_3) have been reported [19–22]. $CuCu_3V_4O_{12}$ demonstrates the rattling of the 12-coordinated loosely bound Cu^{2+} at the A site. For $MnMn_3Mn_4O_{12}$, it exhibits spin-induced ferroelectricity with a strong magnetoelectric effect. In this paper, a TM-only quadruple perovskite $MnCu_3Mn_4O_{12}$ (MCMO) with the charge combination of $Mn^{2+}Cu^{2+}{}_3Mn^{4+}{}_4O_{12}$ was prepared under high-pressure and high-temperature

---

[*] qfangzhang@gmail.com
[†] ywlong@iphy.ac.cn

conditions. The crystal structure, charge states of cations, magnetic, magnetotransport, and specific heat properties were investigated in detail. By comparison with the counterpart CCMO, we found that the *A*-site Mn^{2+} ions play an important role in the magnetic and electrical properties in MCMO.

II. EXPERIMENTAL METHODS

Reagent-grade (>99.9%) MnO, CuO, and MnO_2 powders were used as starting materials to prepare the black polycrystalline sample of MCMO. These reactants at a 1:3:4 mol ratio were finely mixed and ground in an agate mortar and then charged into a gold capsule 2.0 mm in diameter and 3.0 mm in length. The capsule was compressed to 17 GPa and heated to 1373 K for 30 min using a Walker-type double-stage high-pressure apparatus. The powder x-ray diffraction (XRD) was performed at RT on a Huber diffractometer with Cu-$K\alpha_1$ ($\lambda = 1.5406$ Å) radiation at 40 kV and 30 mA to identify sample quality and crystal structure. The XRD data were collected in the 2θ range from 10 ° to 100 ° with a step interval of 0.005 °. For structural refinement, the data were analyzed by the Rietveld method through the GSAS program [23]. The valence states of Cu and Mn were investigated by soft x-ray absorption spectroscopy (XAS) measurements at the National Synchrotron Radiation Research Center in Taiwan. The Cu-$L_{2,3}$ and Mn-$L_{2,3}$ XAS were recorded at beamline 11A using total electron yield mode at RT. CuO and MnO single crystals were measured simultaneously for energy calibrations at the Cu- and Mn-$L_{2,3}$ edges, respectively. Magnetic susceptibility and magnetization measurements were conducted using a commercial superconducting quantum interference device magnetometer (MPMS3, Quantum Design). The dc magnetic susceptibility data were recorded under zero-field-cooled (ZFC) and field-cooled (FC) modes over the temperature range of 2−380 K with an applied field of 0.1 T. The field-dependent isothermal magnetization at different temperatures of 380, 300, 150, and 2 K were obtained under fields varying from −7 to +7 T. The heat capacity, resistance, and MR were measured using a physical property measurement system (PPMS-9T, Quantum Design). The applied magnetic field was perpendicular to the electric current for MR measurement.

The first-principles calculations were performed with the plane-wave code VASP [24,25] using the projector-augmented-wave method [26]. The exchange and correlation effects were described within the generalized gradient approximation with Perdew-Burke-Ernzerhof parametrization [27]. A cutoff energy of 520 eV for MCMO was adopted for the plane-wave expansion of the electronic wave function. The Brillouin zone integration using the Γ-center scheme was sampled with 7×7×7 k-point grids during the geometry optimizations and static electronic structure calculations for MCMO. The lattice constant was fixed as the experimental data, and all atoms were fully relaxed, with residual forces $< 0.005\,\mathrm{eV/Å}$ per atom and the electron energy convergence criteria of 1×10^{-6} eV. Furthermore, due to the well-known limitations of standard density functional theory (DFT) in describing the electronic structure of strongly correlated compounds, the hybrid functional method of HSE06 (suitable mixing between DFT and Hartree-Fock theory) was adopted to more accurately describe the energy and electronic structure of MCMO.

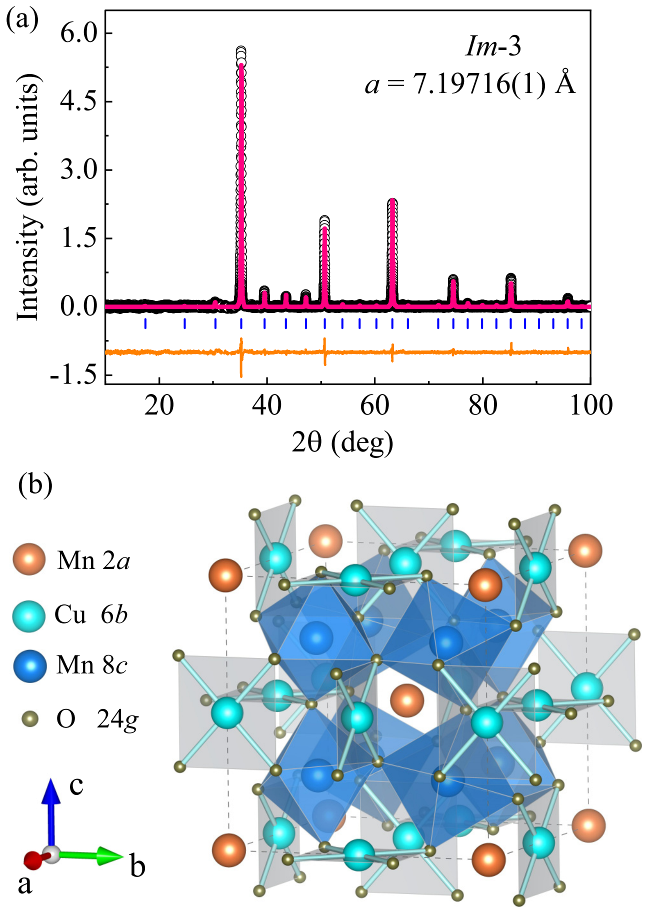

FIG. 1. (a) X-ray diffraction (XRD) pattern and the Rietveld refinement results of MCMO obtained at room temperature (RT). The observed (circles), calculated (pink line), and difference (bottom line) profiles are shown. The blue ticks indicate the allowed Bragg reflections with space group *Im*-3. (b) Crystal structure of *A*-site ordered quadruple perovskite MCMO. The corner-sharing MnO_6 octahedral connections and spatially isolated CuO_4 squares are shown.

III. RESULTS AND DISCUSSION

Figure 1(a) displays the XRD pattern and the structural refinements of MCMO. All the diffraction peaks can be indexed based on a cubic lattice. The Rietveld analysis demonstrates that the compound crystallizes in an $AA'_3B_4O_{12}$-type *A*-site-ordered quadruple perovskite structure with a space group *Im*-3 [see Fig. 1(b)], which is isotypic to that of CCMO [16]. As shown later, the charge format of MCMO is $Mn^{2+}Cu_3^{2+}Mn_4^{4+}O_{12}$. In the determined *Im*-3 symmetry, the *A*-site magnetic Mn^{2+} ion locates at the Wyckoff position 2*a* (0, 0, 0) with 12-coordinated oxygen atoms, the *A*′-site Cu^{2+} at the position 6*b* (0, 0.5, 0.5) with square-planar CuO_4 coordination, the *B*-site Mn^{4+} at the position 8*c* (0.25, 0.25, 0.25) with MnO_6 octahedral coordination, and the oxygen at the position 24*g* (0, *y*, *z*). For comparison, we also prepared CCMO and measured the structure and physical properties. Table I lists the refined crystallographic parameters, selected

TABLE I. Refined structure parameters and BVS calculations for MCMO and CCMO. Space group: *Im*-3; atomic sites: Ca/Mn 2*a* (0, 0, 0), Mn 6*b* (0, 0.5, 0.5), Mn 8*c* (0.25, 0.25, 0.25), and O 24*g* (0, *y*, *z*). The BVS values (V_i) were calculated using the formula $V_i = \sum_j S_{ij}$, and $S_{ij} = \exp[(r_0 - r_{ij})/0.37]$. The value of $r_0 = 1.790$ for Mn_{2a}, $r_0 = 1.679$ for Cu and $r_0 = 1.753$ for Mn_{8c}. For Mn_{2a}, 12-coordinated oxygen atoms were used. For Cu, 12-coordinated oxygen atoms were used. For Mn_{8c}, 6-coordinated oxygen atoms were used.

Parameter	CCMO	Parameter	MCMO
a (Å)	7.21946(1)	*a* (Å)	7.19716(1)
O_y	0.182(2)	O_y	0.183(5)
O_z	0.304(2)	O_z	0.297(6)
U_{iso} (Ca) (100 × Å^2)	0.02(6)	U_{iso} (Mn) (100 × Å^2)	3.50(5)
U_{iso} (Cu) (100 × Å^2)	1.18(1)	U_{iso} (Cu) (100 × Å^2)	0.83(2)
U_{iso} (Mn) (100 × Å^2)	0.99(1)	U_{iso} (Mn) (100 × Å^2)	0.72(2)
U_{iso} (O) (100 × Å^2)	0.61(4)	U_{iso} (O) (100 × Å^2)	0.92(7)
Cu-O (×4 Å)	1.930(4)	Cu-O (×4 Å)	1.967(2)
BVS (Cu)	2.31	BVS (Cu)	2.16
Mn-O (×6 Å)	1.911(5)	Mn_{8c}-O (×6 Å)	1.891(6)
BVS (Mn)	3.91	BVS (Mn_{8c})	4.13
∠Mn-O-Mn (deg)	141.7(2)	∠Mn_{8c}-O-Mn_{8c} (deg)	143.8(1)
∠Cu-O-Mn (deg)	109.0(7)	∠Cu-O-Mn_{8c} (deg)	107.7(2)
R_{wp} (%)	2.54	R_{wp} (%)	2.30
R_p (%)	1.52	R_p (%)	1.51

bond lengths, and bond angles, etc., for these two isostructural compounds. The lattice parameter of MCMO (7.19716 Å) is slightly smaller than that of CCMO (7.21946 Å), in agreement with the reduced ionic size of Mn^{2+} related to Ca^{2+} [28]. According to the refined bond lengths of MCMO, the bond valence sum (BVS) calculations suggest the valence states to be +1.66 for the *A*-site Mn, +2.16 for the *A*′-site Cu, and +4.13 for the *B*-site Mn, implying the formation of a $Mn^{2+}Cu_3^{2+}Mn_4^{4+}O_{12}$ charge combination, as will be further confirmed by XAS measurement. As shown in Table I, the BVS values for Cu and *B*-site Mn are similar in MCMO and CCMO. However, the calculated BVS value for the *A*-site Mn is somewhat less than an expected Mn^{2+} state because of the underbonded effect of Mn^{2+} in the oversized AO_{12} icosahedral cages. As a result, the *A*-site Mn atom in MCMO exhibits a huge thermal displacement parameter ($U_{iso} \approx 0.035$ Å^2), which is larger than that of the Ca atom in CCMO by two orders of magnitude at RT. This observation reveals the active thermal oscillation of the small Mn^{2+} in the oversized icosahedral cages, as observed for the *A*-site magnetic ions in TM-only quadruple perovskite oxides $MnCu_3V_4O_{12}$ and $CuCu_3V_4O_{12}$ [19,20].

To accurately identify the valence states of Cu and Mn in MCMO, the soft XAS at the $L_{2,3}$ edge of 3*d* TM ions was performed, which is widely known to be element specific and sensitive to the valence states [29,30] and the coordination environments [31,32] of 3*d* TM elements. Figure 2(a) shows the Cu-$L_{2,3}$ XAS of MCMO together with $CaCu_3Ti_4O_{12}$ (CCTO) as a Cu^{2+} reference in square-planar coordination [33]. The Cu-$L_{2,3}$ spectrum of MCMO has almost identical energy position and spectral profile as those of CCTO, indicating the presence of a Cu^{2+} state. Figure 2(b) shows the Mn-$L_{2,3}$ XAS of MCMO, along with MnO and $SrMnO_3$ as Mn^{2+} and Mn^{4+} references, respectively [34]. The MCMO spectrum can be well reproduced by a simple superposition of MnO and

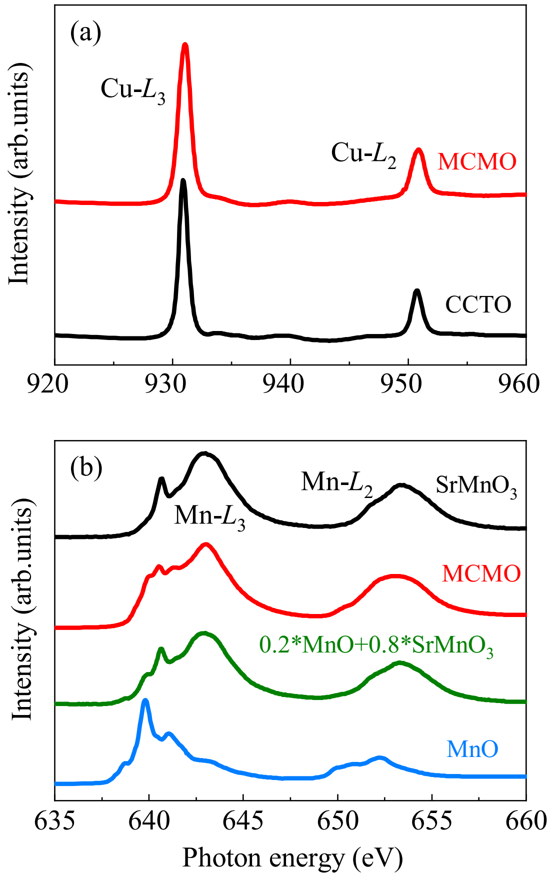

FIG. 2. (a) The Cu-$L_{2,3}$ x-ray absorption spectroscopy (XAS) spectra of MCMO (red) together with related reference CCTO from Ref. [33]. (b) The Mn-$L_{2,3}$ XAS spectra of MCMO (red) together with related references $Mn^{2+}O$ and $SrMn^{4+}O_3$ for comparison. The green line stands for a simple superposition of MnO and $SrMnO_3$ with a 1:4 ratio.

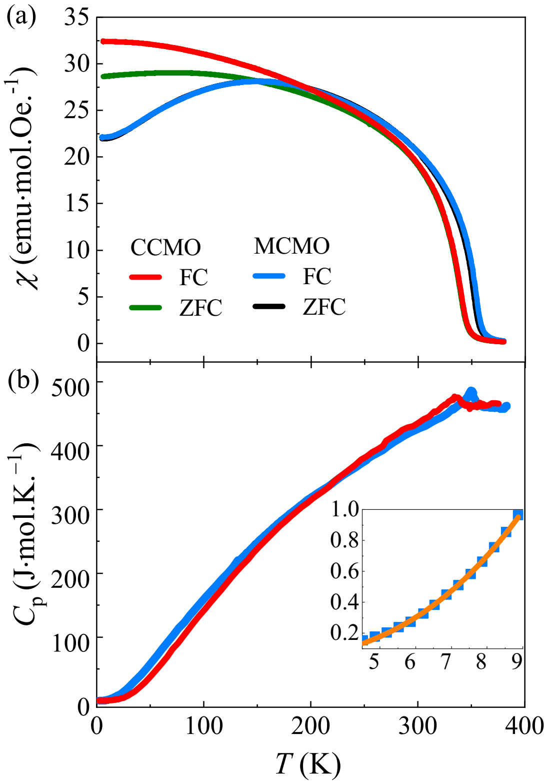

FIG. 3. Temperature dependence of (a) magnetic susceptibility measured at 0.1 T, and (b) specific heat of MCMO and CCMO measured in the temperature range of 2−380 K. The inset shows the low-temperature fitting result for MCMO between 4.5 and 9 K using the formula $C_p = \beta T^3 + \alpha T^{3/2}$.

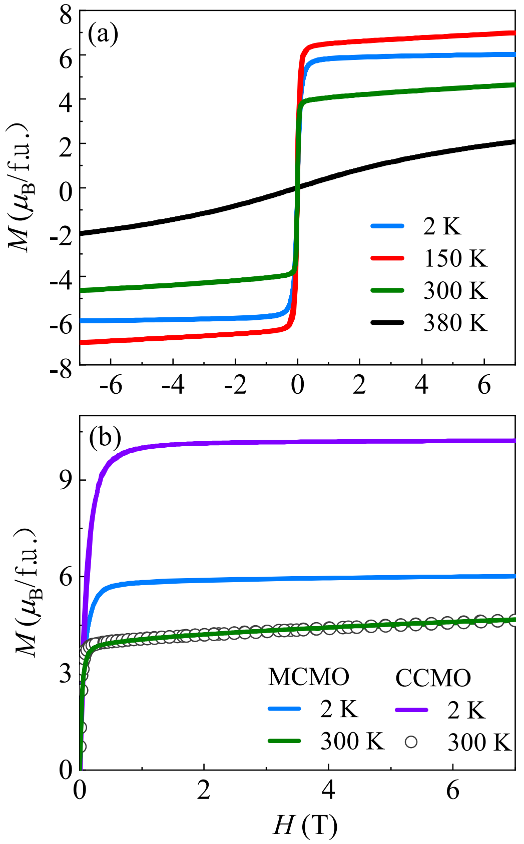

FIG. 4. Field-dependent isothermal magnetization curves measured at (a) some selected temperatures from −7 to 7 T for MCMO, and (b) 2 and 300 K from 0 to 7 T for MCMO and CCMO.

$SrMnO_3$ spectra at a ratio of 1:4. Consequently, the XAS results indicate that the appropriate charge configuration of MCMO is $Mn^{2+}Cu_3^{2+}Mn_4^{4+}O_{12}$, as suggested by BVS calculations. The current MCMO provides a rare example where Mn^{2+} and Mn^{4+} are orderly distributed at the A and B sites in a perovskite-type oxide, respectively.

Figure 3(a) shows the temperature-dependent magnetic susceptibility of CCMO and MCMO measured at 0.1 T. As reported previously, CCMO shows a sharp FiM phase transition at $T_C \approx 355$ K. A similar transition is also found to occur in MCMO, but the T_C is enhanced up to ∼365 K. The semiempirical Goodenough-Kanamori-Anderson (GKA) rules predict an antiferromagnetic (AFM) interaction via a 180° $Mn^{4+}(3d^3)$-O-$Mn^{4+}(3d^3)$ or a 90° $Cu^{2+}(3d^9)$-O-$Mn^{4+}(3d^3)$ superexchange pathway [35–37]. Compared with CCMO which possesses the Cu^{2+}-O-Mn^{4+} bond angle of ∼109.0°, the Cu^{2+}-O-Mn^{4+} bond angle observed in the current MCMO is reduced to 107.7°. Although the Mn^{4+}-O-Mn^{4+} superexchange pathway in CCMO (141.7°) is more bent than that in MCMO (143.8°), the latter shows a higher spin order temperature than the former. This behavior indicates that the $Cu^{2+}(\uparrow)Mn^{4+}(\downarrow)$ AFM (or FiM) interactions should dominate the magnetic ordering temperature at T_C. Different from the single magnetic transition observed in CCMO, where the susceptibility tends to be saturated below the T_C with a small separation between ZFC and FC curves at low temperature, the susceptibility of MCMO shows a broadening dome ∼200 K, below which the susceptibility starts to gradually decrease and a saturated plateau emerges at the temperatures <∼ 10 K [see Fig. 3(a)]. Moreover, the ZFC and FC susceptibility curves of MCMO almost overlap with each other in the whole temperature region we measured. These observations indicate that the A-site Mn^{2+} magnetic ions may start to participate in spin interactions with temperature down to ∼200 K.

Figure 4(a) shows the field-dependent isothermal magnetization behaviors measured at some representative temperatures for MCMO. Below T_C, there exist clear magnetic hysteresis features with very small coercive fields (e.g., only 10 Oe at 2 K), suggesting soft ferromagnetism. Corresponding to the dome-type magnetic susceptibility, the saturated moment observed at 150 K (7.0 μ_B/f.u.) is larger than that at 2 K (6.0 μ_B/f.u.), demonstrating that the participation of A-site Mn^{2+} spins decreases the total saturated moment. As is well known, a $Cu^{2+}(\uparrow)Mn^{4+}(\downarrow)$ FiM coupling is determined in CCMO. As presented in Fig. 3(a), MCMO and CCMO display similar high-temperature magnetic phase transitions. As shown in Fig. 4(b), both compounds possess nearly identical saturated moment at 300 K (4.65 μ_B/f.u.). These results illustrate that a similar $Cu^{2+}(\uparrow)Mn^{4+}(\downarrow)$ FiM phase transition would take place at $T_C \approx 365$ K in MCMO without the contribution of A-site Mn^{2+} spins. However, the saturated moment of MCMO measured at 2 K (6.0 μ_B/f.u.) is much less than that of CCMO (10.0 μ_B/f.u.)

by $\sim 4.0\ \mu_{\mathrm{B}}/\mathrm{f.u.}$ [see Fig. 4(b)]. This difference is comparable with the theoretical spin moment for a localized high-spin Mn^{2+} ion ($5.0\ \mu_{\mathrm{B}}/\mathrm{f.u.}$). Considering the A-site Mn^{2+} magnetic contribution, the spin ground state of MCMO most probably is a FiM $\mathrm{Mn}^{2+}(\uparrow)\mathrm{Cu}^{2+}(\uparrow)\mathrm{Mn}^{4+}(\downarrow)$. Note that a collinear $\mathrm{Mn}^{2+}(\uparrow)\mathrm{Cu}^{2+}(\uparrow)\mathrm{Mn}^{4+}(\downarrow)$ FiM alignment gives rise to the saturated moment to be $4.0\ \mu_{\mathrm{B}}/\mathrm{f.u.}$, which is somewhat less than the experimental value measured at 2 K ($6.0\ \mu_{\mathrm{B}}/\mathrm{f.u.}$). This result may mean that some spins are canting. Anyway, the current MCMO displays double magnetic transitions. One is a sharp $\mathrm{Cu}^{2+}(\uparrow)\mathrm{Mn}^{4+}(\downarrow)$ FiM phase transition occurring between the A'-site Cu^{2+} and the B-site Mn^{4+} ions at $T_{\mathrm{C}} \approx 365\,\mathrm{K}$. The other is a sluggish spin ordering of the A-site Mn^{2+} ions in a broadening temperature region. The presence of a low-temperature plateau observed in the susceptibility $<10\,\mathrm{K}$ might be indicative of the complete development for the A-site spin ordering. Based on the GKA rules, a FM interaction is predicted to occur between the A-site Mn^{2+} and the A'-site Cu^{2+} with $3d^5(t_{2g}^5)$ and $3d^9(t_{2g}^6e_g^3)$ electronic configurations, respectively, via the Mn^{2+}-O-Cu^{2+} superexchange pathways. In contrast, an AFM interaction is expected to occur between the A-site Mn^{2+} (t_{2g}^5) and the B-site Mn^{4+} (t_{2g}^3) via the Mn^{2+}-O-Mn^{4+} superexchange pathways. The formation of dome-type susceptibility behavior in MCMO may arise from the competing coupling between the Mn^{2+}-O-Cu^{2+} FM and the Mn^{2+}-O-Mn^{4+} AFM interactions. The magnetism of MCMO is reminiscent of the magnetic properties observed in Nd/Ho/Er/Tb$\mathrm{Cu_3(Mn_3Fe)O_{12}}$ [38,39], where similar broadening dome-type susceptibility features are also found to occur since the A-site rare-earth ions undergo long-range magnetic orderings and antiferromagnetically couple with the B-site Mn^{4+} magnetic moments.

Figure 3(b) shows the temperature dependence of specific heat of MCMO and CCMO in the temperature range of 2–380 K. Corresponding to the FiM transitions, one can also find the related λ-type anomalies near the Curie temperatures. Since the A-site Mn^{2+} spins order sluggishly in a wide temperature region (~10–200 K), there is no apparent anomaly occurring in the specific heat of MCMO. However, when we compare the specific heat data between CCMO and MCMO, the latter are slightly larger than the former in 10–200 K, in coherence with the sluggish spin ordering of A-site Mn^{2+} spins. Below 10 K, the specific heat data of MCMO can be well fitted by the formula $C_p = \beta T^3 + \alpha T^{3/2}$ [see the inset of Fig. 3(b)]. Here, the T^3 term originates from the phonon and AFM contributions, while the $T^{3/2}$ term represents the contribution of FM excitation, as expected from the possible $\mathrm{Mn}^{2+}(\uparrow)\mathrm{Cu}^{2+}(\uparrow)\mathrm{Mn}^{4+}(\downarrow)$ FiM ground state. The fitting yields the coefficients $\beta = 1.31(2) \times 10^{-3}\,\mathrm{J/mol\,K^4}$ and $\alpha = 1.41(5) \times 10^{-3}\,\mathrm{J/mol\,K^{5/2}}$.

A-site Mn^{2+} ions play a striking role on the magnetism of MCMO. We now present their effects on electrical transport. Figure 5(a) shows the temperature dependence of electrical resistivity ρ measured at 0 T for MCMO and CCMO. Both compounds have comparable ρ values at higher temperatures (e.g., $>250\,\mathrm{K}$), when the A-site Mn^{2+} spins do not take part in a long-range spin ordering. Once the Mn^{2+} spins start to become ordering, however, the resistivity of MCMO is significantly suppressed. Specifically, the resistivity of CCMO monotonously increases with decreasing temperature. In contrast, a kink is found to occur ~200 K in MCMO, and the magnitude of ρ is nearly constant below the onset ordering temperature for A-site Mn^{2+} spins. Note that there is no resistivity anomaly occurring around the FiM Curie temperatures in both CCMO and MCMO. Just like CCMO, the present MCMO also exhibits considerable MR behavior without introducing Mn^{3+}-O-Mn^{4+} double exchange interactions. Figure 5(b) depicts the temperature-dependent resistivity measured at 0 and 8 T for MCMO. Obviously, the magnetic field can suppress the resistivity and lead to negative MR $\{= 100\% \times [\rho(H)\text{-}\rho(0)]/\rho(0)\}$ behavior. As shown in Fig. 5(b), the calculated MR values between 0 and 8 T are negligible above T_{C}, while they start to sharply decrease below this FiM critical temperature with the occurrence of a clear kink ~200 K due to the A-site Mn^{2+} spin ordering.

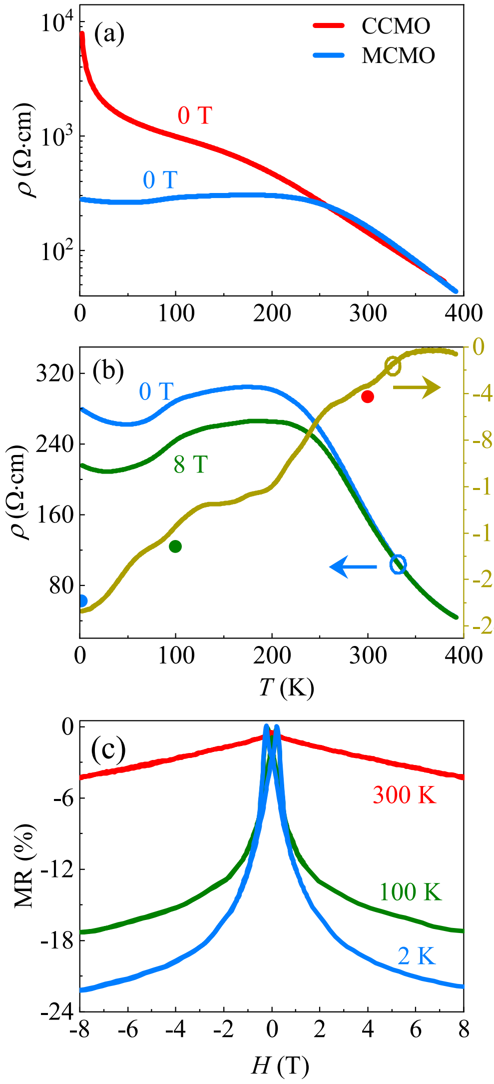

FIG. 5. Temperature dependence of (a) resistivity at 0 T for MCMO and CCMO, and (b) resistivity measured at 0 and 8 T for MCMO and the calculated magnetoresistance (MR) between these two fields. (c) Field-dependent MR effects measured at fixed temperatures for MCMO. The solid circles in (b) show the MR values obtained at 8 T and fixed temperatures from (c).

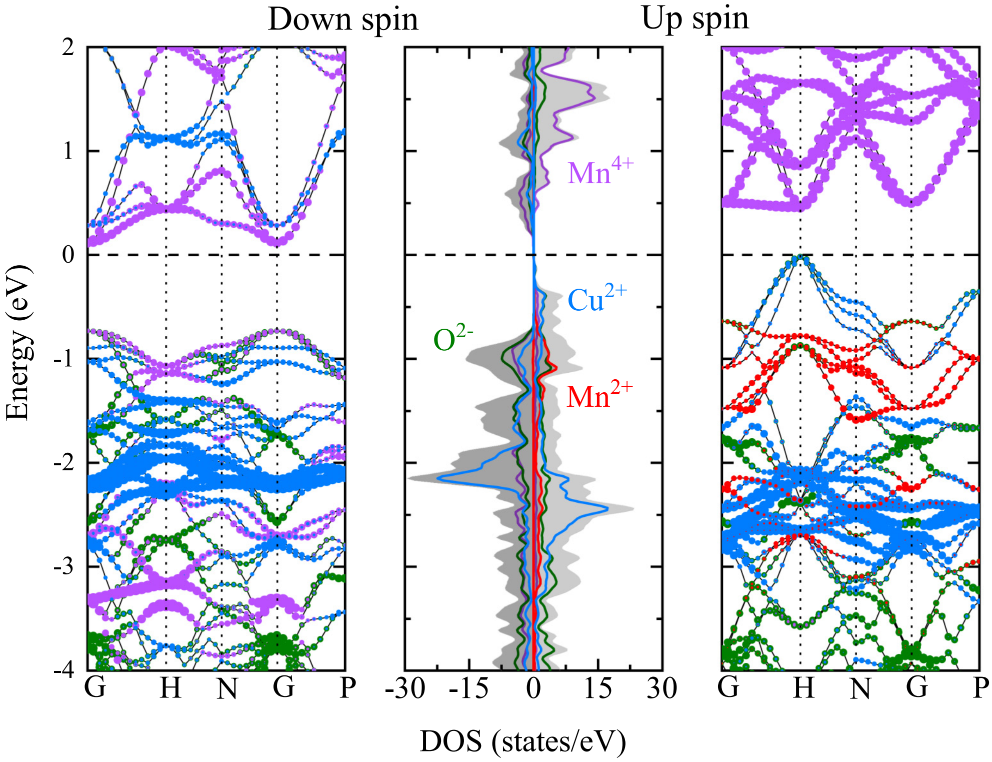

FIG. 6. First-principles numerical results for the band structures and partial density of states (DOS) of MCMO using HSE06.

Furthermore, Fig. 5(c) shows the magnetic-field-dependent negative MR values of MCMO measured at some fixed temperatures (300, 100, and 2 K) below T_C. The MR sharply decreases with the magnetic field in ±2 T, suggesting significant low-field MR effects. The calculated absolute value of MR is ∼18% at 2 K and 2 T and increases to 22% with the field up to 8 T. It is worth noting that the MR values measured by field- and temperature-scan methods are comparable, as demonstrated in Fig. 5(b).

To gain a deeper insight into the *A*-site spin tuned magnetic and electronic properties of MCMO, the hybrid density functional of HSE06 calculations were carried out for different collinear magnetic configurations, i.e., the FM $Mn^{2+}(\uparrow)Cu^{2+}(\uparrow)Mn^{4+}(\uparrow)$ and the FiM $Mn^{2+}(\uparrow)Cu^{2+}(\uparrow)Mn^{4+}(\downarrow)$, $Mn^{2+}(\uparrow)Cu^{2+}(\downarrow)Mn^{4+}(\uparrow)$, and $Mn^{2+}(\uparrow)Cu^{2+}(\downarrow)Mn^{4+}(\downarrow)$. The calculations always converge to the FiM $Mn^{2+}(\uparrow)Cu^{2+}(\uparrow)Mn^{4+}(\downarrow)$ ground state irrespective of the initial configuration. The calculated magnetic moments inside the muffin tin spheres are 4.51, 0.49, −2.63, and 0.046 μ_B/f.u. for Mn^{2+}, Cu^{2+}, Mn^{4+}, and O^{2-}ions, respectively. The reduction from the ideal value results from hybridization with the O 2*p* state. The total magnetic moment is −3.99 μ_B/f.u., which is comparable with the experimentally observed saturated magnetic moment at 2 K.

Figure 6 shows the calculated electronic band structures and DOS with the HSE06 to MCMO. The calculated energy gaps are 0.48 eV for spin-up and 0.85 eV for spin-down channels. Note that the major contributions to the total DOS around the Fermi level are attributed to the Cu 3*d* orbitals in spin-up channels, which strongly hybridize with the *A*-site Mn 3*d* and O 2*p* orbitals. This is very different from the case in CCMO, where the Ca contributions emerge >6 eV above the Fermi level and O 2*p* orbitals have little contribution in this energy zone [40]. However, in the current MCMO, because the *A*-site Mn 3*d* orbitals locate near the Fermi energy and have a considerable hybridization with the Cu 3*d* and O 2*p* orbitals, the *A*-site Mn^{2+} spins can participate in the Mn^{2+}-O-Cu^{2+} and Mn^{2+}-O-Mn^{4+} spin and electrical transport pathways. As a result, the magnetism and transport properties of MCMO can be well tuned by the *A*-site TM ions.

IV. CONCLUSIONS

In summary, we have succeeded in preparing a TM-only quadruple perovskite MCMO at 17 GPa and 1373 K. The charge combination based on the BVS and XAS measurements is confirmed to be $Mn^{2+}Cu_3^{2+}Mn_4^{4+}O_{12}$. Due to the underbonded effect of Mn^{2+} in the oversized AO_{12} icosahedral cages, an unusually large thermal displacement parameter is observed. As revealed by magnetization and heat capacity measurements, MCMO undergoes a long-range FiM transition around $T_C \approx 365$ K arising from the $Cu^{2+}(\uparrow)Mn^{4+}(\downarrow)$ spin coupling. As the temperature decreases to ∼200 K, the *A*-site Mn^{2+} spins start to experience a sluggish spin ordering, leading to the formation of a possible $Mn^{2+}(\uparrow)Cu^{2+}(\uparrow)Mn^{4+}(\downarrow)$ FiM ground state. The *A*-site spin ordering causes a broadening dome in magnetic susceptibility and suppresses the magnitude of resistivity significantly. First-principles calculations reveal that the *A*-site Mn^{2+} 3*d* orbitals locate near the Fermi energy and have a considerable hybridization with the Cu 3*d* and O 2*p* orbitals. As a result, the *A*-site TM ions play an important role in the magnetism and electrical transport properties in the current MCMO.

ACKNOWLEDGMENTS

This paper was supported by the National Key R&D Program of China (Grants No. 2021YFA1400300, No. 2018YFE0103200, and No. 2018YFA0305700), the National Natural Science Foundation of China (Grants No. 11934017, No. 11921004, and No. 51772324), the Beijing Natural Science Foundation (Grant No. Z200007), and the Chinese Academy of Sciences (Grant No. XDB33000000). We acknowledge support from the Max Planck-POSTECH-Hsinchu Center for Complex Phase Materials.

---

[1] Y. W. Long, N. Hayashi, T. Saito, M. Azuma, S. Muranaka, and Y. Shimakawa, Nature (London) **458**, 60 (2009).

[2] Y. Long, T. Saito, T. Tohyama, K. Oka, M. Azuma, and Y. Shimakawa, Inorg. Chem. **48**, 8489 (2009).

[3] Y. Long and Y. Shimakawa, New J. Phys. **12**, 063029 (2010).

[4] I. Yamada, K. Shiro, H. Etani, S. Marukawa, N. Hayashi, M. Mizumaki, Y. Kusano, S. Ueda, H. Abe, and T. Irifune, Inorg. Chem. **53**, 10563 (2014).

[5] I. Yamada, H. Etani, M. Murakami, N. Hayashi, T. Kawakami, M. Mizumaki, S. Ueda, H. Abe, K.-D. Liss, A. J. Studer, T. Ozaki, S. Mori, R. Takahashi, and T. Irifune, Inorg. Chem. **53**, 11794 (2014).

[6] I. Yamada, M. Murakami, N. Hayashi, and S. Mori, Inorg. Chem. **55**, 1715 (2016).

[7] I. Yamada, K. Takata, N. Hayashi, S. Shinohara, M. Azuma, S. Mori, S. Muranaka, Y. Shimakawa, and M. Takano, Angew. Chem., Int. Ed. **47**, 7032 (2008).

[8] C. C. Homes, T. Vogt, S. M. Shapiro, S. Wakimoto, and A. P. Ramirez, Science **293**, 673 (2001).

[9] X. Wang, Y. S. Chai, L. Zhou, H. B. Cao, C. D. Cruz, J. Y. Yang, J. H. Dai, Y. Y. Yin, Z. Yuan, S. J. Zhang, R. Z. Yu, M. Azuma, Y. Shimakawa, H. M. Zhang, S. Dong, Y. Sun, C. Q. Jin, and Y. W. Long, Phys. Rev. Lett. **115**, 087601 (2015).

[10] L. Zhou, J. H. Dai, Y. S. Chai, H. M. Zhang, S. Dong, H. B. Cao, S. Calder, Y. Y. Yin, X. Wang, X. D. Shen, Z. H. Liu, T. Saito, Y. Shimakawa, H. Hojo, Y. Ikuhara, M. Azuma, Z. W. Hu, Y. Sun, C. Q. Jin, and Y. W. Long, Adv. Mater. **29**, 1703435 (2017).

[11] X. Miao, L. Zhang, L. Wu, Z. Hu, L. Shi, and S. Zhou, Nat. Commun. **10**, 3809 (2019).

[12] S. Yagi, I. Yamada, H. Tsukasaki, A. Seno, M. Murakami, H. Fujii, H. Chen, N. Umezawa, H. Abe, N. Nishiyama, and S. Mori, Nat. Commun. **6**, 8249 (2015).

[13] X. Ye, S. Song, L. Li, Y. Chang, S. Qin, Z. Liu, Y. Huang, J. Zhou, L. Zhang, C. Dong, C. Pao, H. Lin, C. Chen, Z. Hu, J. Wang, and Y. Long, Chem. Mater. **33**, 9295 (2021).

[14] Y. Long, Chin. Phys. B **25**, 078108 (2016).

[15] H. Shiraki, T. Saito, T. Yamada, M. Tsujimoto, M. Azuma, H. Kurata, S. Isoda, M. Takano, and Y. Shimakawa, Phys. Rev. B **76**, 140403 (2007).

[16] Z. Zeng, M. Greenblatt, M. A. Subramanian, and M. Croft, Phys. Rev. Lett. **82**, 3164 (1999).

[17] J. Sánchez-Benítez, J. A. Alonso, M. J. Martínez-Lope, A. de Andres, and M. T. Fernández-Díaz, Inorg. Chem. **49**, 5679 (2010).

[18] J. Sánchez-Benítez, P. Kayser, A. Morales-García, M. J. Martínez-Lope, F. J. Mompeán, J. Xu, Z. Jin, and J. A. Alonso, J. Phys. Chem. C **118**, 9652 (2014).

[19] Y. Akizuki, I. Yamada, K. Fujita, N. Nishiyama, T. Irifune, T. Yajima, H. Kageyama, and K. Tanaka, Inorg. Chem. **52**, 11538 (2013).

[20] Y. Akizuki, I. Yamada, K. Fujita, K. Taga, T. Kawakami, M. Mizumaki, and K. Tanaka, Angew. Chem. Int. Ed. **54**, 10870 (2015).

[21] S. V. Ovsyannikov, A. M. Abakumov, A. A. Tsirlin, W. Schnelle, R. Egoavil, J. Verbeeck, G. Van Tendeloo, K. V. Glazyrin, M. Hanfland, and L. Dubrovinsky, Angew. Chem., Int. Ed. **52**, 1494 (2013).

[22] J. Cong, K. Zhai, Y. Chai, D. Shang, D. D. Khalyavin, R. D. Johnson, D. P. Kozlenko, S. E. Kichanov, A. M. Abakumov, A. A. Tsirlin, L. Dubrovinsky, X. Xu, Z. Sheng, S. V. Ovsyannikov, and Y. Sun, Nat. Commun. **9**, 2996 (2018).

[23] A. C. Larson and R. B. Von Dreele, General structure analysis system (GSAS), Report No. LAUR 86-748 (Los Alamos National Laboratory, Los Alamos, NM, 1994).

[24] G. Kresse and J. Furthmuller, Phys. Rev. B **54**, 11169 (1996).

[25] G. Kresse and J. Furthmuller, Comp. Mater. Sci. **6**, 15 (1996).

[26] G. Kresse and D. Joubert, Phys. Rev. B **59**, 1758 (1999).

[27] J. P. Perdew, K. Burke, and M. Ernzerhof, Phys. Rev. Lett. **77**, 3865 (1996).

[28] R. D. Shannon, Acta Cryst. A **32**, 751 (1976).

[29] L. H. Tjeng, C. T. Chen, and S. W. Cheong, Phys. Rev. B **45**, 8205 (1992).

[30] T. Burnus, Z. Hu, H. H. Hsieh, V. L. J. Joly, P. A. Joy, M. W. Haverkort, H. Wu, A. Tanaka, H. J. Lin, C. T. Chen, and L. H. Tjeng, Phys. Rev. B **77**, 125124 (2008).

[31] T. Burnus, Z. Hu, H. Wu, J. C. Cezar, S. Niitaka, H. Takagi, C. F. Chang, N. B. Brookes, H. J. Lin, L. Y. Jang, A. Tanaka, K. S. Liang, C. T. Chen, and L. H. Tjeng, Phys. Rev. B **77**, 205111 (2008).

[32] S. Nemrava, D. A. Vinnik, Z. W. Hu, M. Valldor, C. Y. Kuo, D. A. Zherebtsov, S. A. Gudkova, C. T. Chen, L. H. Tjeng, and R. Niewa, Inorg. Chem. **56**, 3861 (2017).

[33] X. Ye, Z. Liu, W. Wang, Z. Hu, H.-J. Lin, S.-C. Weng, C.-T. Chen, R. Yu, L.-H. Tjeng, and Y. Long, J. Phys.: Condens. Matter **32**, 075701 (2020).

[34] D. H. Kim, E. Lee, H. W. Kim, S. Kolesnik, B. Dabrowski, C.-J. Kang, M. Kim, B. I. Min, H.-K. Lee, J. Y. Kim, and J. S. Kang, Phys. Rev. B **91**, 075113 (2015).

[35] P. W. Anderson, Phys. Rev. **79**, 350 (1950).

[36] J. B. Goodenough, Phys. Rev. **100**, 564 (1955).

[37] J. Kanamori, J. Phys. Chem. Solids **10**, 87 (1959).

[38] J. Sánchez-Benítez, P. Kayser, M. J. Martínez-Lope, C. de la Calle, M. Retuerto, M. T. Fernandez-Díaz, and J. A. Alonso, J. Phys.: Conf. Ser. **325**, 012002 (2011).

[39] P. Kayser, M. J. Martínez-Lope, M. Retuerto, J. Sánchez-Benítez, M. T. Fernández-Díaz, and J. A. Alonso, Dalton Trans. **41**, 10670 (2012).

[40] X.-J. Liu, H.-P. Xiang, P. Cai, X.-F. Hao, Z.-J. Wu, and J. Meng, J. Mater. Chem. C **16**, 4243 (2006).